CrossMark

J. Fluid Mech. (2017), *vol.* 823, R4, doi:10.1017/jfm.2017.389



JFM RAPIDS
journals.cambridge.org/rapids

Relaxation drag history of shock accelerated microparticles

Ankur D. Bordoloi[1,†], **Adam A. Martinez**[1] **and Katherine Prestridge**[1]

[1]Physics Division, Los Alamos National Laboratory, Los Alamos, NM 87545, USA

(Received 4 April 2017; revised 22 May 2017; accepted 29 May 2017;
first published online 21 June 2017)

Experimental measurements of the displacements of shock accelerated microparticles from shortly after shock interaction to the particle relaxation time show time-dependent drag coefficients (C_D) that are much higher than those predicted by quasi-steady and unsteady drag models. Nylon particles with mean diameter of 4 μm, accelerated by one-dimensional normal shocks (Mach number $M_s = 1.2$, 1.3 and 1.4), have measured C_D values that follow a power-law behaviour. The drag is a function of the time-dependent Knudsen number, $Kn^* = M_s/Re_p$, where the particle Reynolds number (Re_p) is calculated using the time-dependent slip velocity. Some portion of the drag can be attributed to quasi-steady forces, but the total drag cannot be predicted by current unsteady force models that are based on the Basset–Boussinesq–Oseen equation and pressure drag. The largest contribution to the total drag is the unsteady component ($C_{D,us}$) until the particle attains $Kn^* \approx 0.5$–1.0, then the unsteady contribution decays. The quasi-steady component ($C_{D,qs}$) increases almost linearly with Kn^*, intersects the $C_{D,us}$ at $Kn^* \approx 2$ and becomes the primary contributor to the drag towards the end of the relaxation zone as $Re_p \to 0$. There are currently no analytical models that are able to predict the nonlinear behaviour of the shock accelerated particles during the relaxation phase of the flow.

Key words: high-speed flow, multiphase and particle-laden flows, shock waves

1. Introduction

Shocked multiphase flows involve complex transfer of mass, momentum and energy between the dispersed and carrier phases. The passage of a shock wave through a multiphase medium causes the particles to first accelerate behind the shock and eventually relax into mechanical and thermal equilibrium with the post-shock carrier phase (Rudinger 1964). The two-phase interactions in the relaxation zone often result in evaporation, deformation and breakup of the dispersed particles as well as modulation of the carrier phase turbulence (Gore & Crowe 1989; Smolders & van Dongen 1992; Strecker & Roth 1994).

† Email address for correspondence: ankur@lanl.gov

© Cambridge University Press 2017

https://doi.org/10.1017/jfm.2017.389 Published online by Cambridge University Press

The physics of particles accelerating behind a shock wave requires an understanding of the drag experienced by individual particles during the relaxation phase. Over the past few decades, the experimental work on unsteady drag behind a shock wave has primarily been limited to the bulk motion of a particle cloud (Rudinger 1970; Murakama & Ishikawa 1978; Miura & Glass 1983; Boiko *et al.* 1997; Geng & Groenig 2000). Rudinger (1970) measured particle drag coefficients (C_D) from the traces of bulk particle trajectories and found the local C_D to be two orders of magnitude larger than the expected values from standard drag equations. They proposed a qualitative model for the drag of the cloud accounting for the nonlinear phase interactions that cause longitudinal and lateral perturbations to individual particles from their mean trajectory. Sommerfeld (1985) measured particle velocity using laser Doppler anemometry and proposed an empirical correlation for particle C_D in the range $50 < Re_p < 500$. Igra & Takayama (1993) measured C_D based on double-exposure holography images for spherical particles placed initially on the shock tube floor. These measurements also showed significantly large unsteady drag coefficients. Jourdan *et al.* (2007) extended the drag measurement of a single particle to the relaxation zone using shadowgraphy and estimated C_D on particles of millimetre size ($d_p = 0.62$–6.5 mm) attached to a spider web. Their measurements for a range of particle densities ($\rho_p = 25$–1096 kg m^{-3}) yielded C_D values over 50 % higher than standard predictions. Sun *et al.* (2005) observed a steep increase in drag for large spheres ($d_p = 80$ mm) suspended on a thin wire during the passage of a shock.

The dynamics of dispersed particles in gas have been studied under various unsteady conditions (Kulick, Fessler & Eaton 1994; Tanaka & Eaton 2010). The total unsteady force (F_p) on a small rigid sphere is modelled using quasi-steady (F_{qs}), inviscid unsteady (F_{iu}, pressure gradient and added mass), viscous unsteady (F_{vu}, Basset history force), gravity (F_g) and lift (F_l) forces (Maxey & Riley 1983; Magnaudet & Eames 2000). Theoretical and empirical models for the forces on shock accelerated particles have been proposed by Miles (1951), Longhorn (1952), Henderson (1976), Saito *et al.* (2007), Loth (2008) and Parmar, Haselbacher & Balachandar (2008, 2009, 2010). Henderson (1976), Loth (2008) and Parmar *et al.* (2010) proposed empirical correlations for the quasi-steady drag on spherical particles in compressible multiphase flows. Parmar *et al.* (2008) and Parmar *et al.* (2009) proposed a model for the inviscid component of drag based on an unsteady force kernel. They showed that the unsteady drag on a particle reaches a peak that is an order of magnitude higher than the standard drag during the passage of the shock across the particle, and this peak is primarily caused by the inviscid unsteady (F_{iu}) force. This model reinforces the observations of Sun *et al.* (2005) but is not extended beyond a very short time period, $O(\tau_s = d_p/u_s)$, compared with the total relaxation time, where τ_s, d_p and u_s are the acoustic time scale, particle diameter and shock speed.

Some progress has been made in modelling unsteady viscous forces. Mei & Adrian (1992) used a linearised asymptotic analysis based on the numerical results by Mei, Lawrencce & Adrian (1991) for small oscillations about a mean flow around a sphere and proposed an approximate model for the Basset history kernel. Parmar, Haselbacher & Balachandar (2011) accounted for the compressibility effects and proposed a model for the linearised Basset–Boussinesq–Oseen (BBO) equation in the limit of $M_p \to 0$ and $Re_p \to 0$ accounting for the history kernel in F_{vu}. The understanding of the viscous unsteady component of drag for shock driven flows is limited to these linearised models, but the unsteady drag on the particle through the relaxation phase is likely to be caused by nonlinear effects.

Many experimental studies observe high drag coefficients for bulk and individual particles, but the physical mechanisms behind the high drag remain unclear. We have

https://doi.org/10.1017/jfm.2017.389 Published online by Cambridge University Press

Parameter	Definition	Value		
Particle density, kg m^{-3}	ρ_p		1140	
Incident Mach number	$M_s = V_s/c$	1.2	1.3	1.4
Post-shock gas velocity, m s^{-1}	u_g	108	160	203
Post-shock gas density, kg m^{-3}	ρ_g	1.2526	1.4151	1.5775
Post-shock gas viscosity, kg m^{-1} s^{-1}	μ_g	2.003×10^{-5}	2.086×10^{-5}	2.167×10^{-5}
Particle Mach number	$M_p = \dfrac{(u_g - u_p)}{c_2}$	0.002–0.3	0.004–0.4	0.04–0.5
Particle Reynolds number	$Re_p = \dfrac{\rho_g d_p (u_g - u_p)}{\mu_g}$	0.31–25.8	0.4–42.3	4.8–56.4
Flow Knudsen number	$Kn = \dfrac{M_{p,max}}{Re_{p,max}} \sqrt{\dfrac{\gamma \pi}{2}}$	0.017	0.014	0.013
Particle volume fraction	C		$\approx 10^{-7}$	

TABLE 1. Experimental parameters and values. Here, the pre-shock speed of sound, $c = 344$ m s^{-1} at 294.8 K. Post-shock properties, including the speed of sound, c_2, are calculated using one-dimensional normal shock relations (Anderson 1990).

designed shock tube experiments to precisely measure particle displacements for shock accelerated microparticles. The effects of compressibility observed by Boiko *et al.* (1997) and Wagner *et al.* (2012) are avoided by keeping the particle Mach number in the subsonic range ($M_p < 0.6$). Unlike most of the previous studies, unsteady drag is calculated for individual particles through particle relaxation.

2. Experimental set-up and methods

Experiments are conducted in a 6.5 m horizontal shock tube (HST) with a 76.2 × 76.2 mm^2 cross-section. The shock tube generates repeatable shock waves using a diaphragmless pneumatic driver that keeps the shock tube free of contamination from diaphragm fragments (Martinez, Orlicz & Prestridge 2015; Mejia-Alvarez *et al.* 2015). Six pressure transducers (PT1–PT6, PCB Piezotronics Inc. Model 113B27), with PT4 being exactly at the centre of the measurement section, are incorporated along the length of the tube to measure shock speed and to trigger the imaging diagnostics. A detailed description of the HST can be found in Martinez *et al.* (2015). The driver pressure is set between 0.14 and 0.4 MPa to obtain incident shock Mach numbers of $M_s = 1.2$, 1.3 and 1.4. Table 1 summarises the detailed experimental parameters for each Mach number.

Nylon particles (TSI 10084) with mean diameter $d_p = 4$ μm and mass density $\rho_p = 1140$ kg m^{-3} are used for all experiments. The particles are driven through a pipe, enter the shock tube through an inlet port with area 484 mm^2 located near the driver and exit through a similar port located near the end of the tube. A fan keeps the average pre-shock speed of a particle to approximately 0.6 m s^{-1}, which is negligibly small compared with the speed of the shock and the post-shock gas. The post-shock

https://doi.org/10.1017/jfm.2017.389 Published online by Cambridge University Press

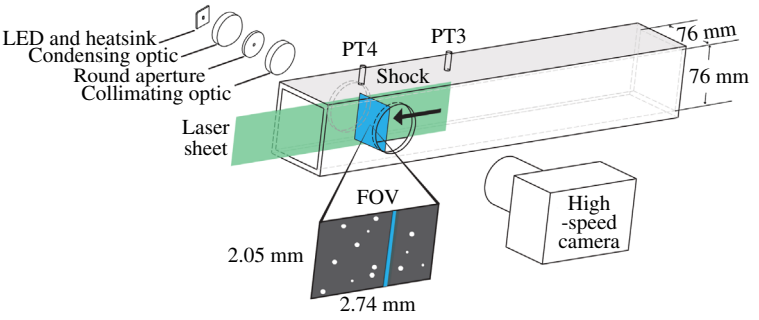


FIGURE 1. Schematic of the test section in the horizontal shock tube. The shock moves from right to left. The inset shows the field of view (FOV) with an example shock position. The camera images the shadowgraph and scattered light from the particles within the laser sheet.

gas velocity (u_g) is estimated based on the Rankine–Hugoniot relationship for normal shocks, and the estimate is confirmed experimentally. The particles are dispersed in a dilute concentration ($C \approx 10^{-7}$) such that there is no particle–particle interaction, and the particles do not affect the post-shock properties of the gas (Rudinger 1964).

The current measurements are conducted in the test section schematically shown in figure 1. Particles are illuminated by four dual-head Nd : YAG 532 nm lasers (Quantel Twins CFR300, repetition rate 15 Hz), each head being timed independently to produce a single pulse of light sheet with a width of 1 mm. The particles and shock are imaged simultaneously at 5.83 m from the driver using an eight-frame SIMD high-speed framing camera positioned orthogonal to the laser sheet. The output laser pulse timing is measured with a photodiode, and particle images are calibrated using a precision chrome-on-glass cross-hair grid (Edmund Optics FA79E-58509). The depth of field of 0.75 mm was measured using a DOF 5-15 target with the camera aperture set at $f/22$ (Martinez *et al.* 2015). The image resolution is 2.14 μm pixel^{-1} at a magnification of 3, and the total field of view is 2.74×2.05 mm^2. The shock position is measured on either frame two or three with a shadowgraph from a pulsed LED light source (Luminus 18A, CBT-120 Green LED).

The absolute shock location and shock speed (V_s) determine when each particle interacts with the shock. We calculate the shock speed using the pressure traces from transducers PT1–PT4 and the position from shadowgraph images. Figure 2(*a*) shows sample pressure traces obtained from transducers PT3 and PT4 for an experiment with $M_s = 1.3$. As the shock wave traverses the transducer head, the pressure signal rises from zero to a maximum value. Assuming that the shock reaches the centre of a transducer when the pressure is half that of the maximum, the shock speed (V_s) is the interval between the two half-peak times and the centre-to-centre distance between transducers PT3 and PT4. The location (x_s) of the shock is obtained for each shot from a shadowgraph image containing the shock wave at a known time, t_s (see figure 2*b*). The band in the shadowgraph (typically 50–150 pixels wide) is caused by diffraction of light about the edge of the shock (Settles 2006). The shock location in figure 2(*b*) is measured by taking a mean intensity along the y-axis after background subtraction and a Gaussian noise filter are applied, giving 0.5 pixel accuracy in the shock location.

https://doi.org/10.1017/jfm.2017.389 Published online by Cambridge University Press

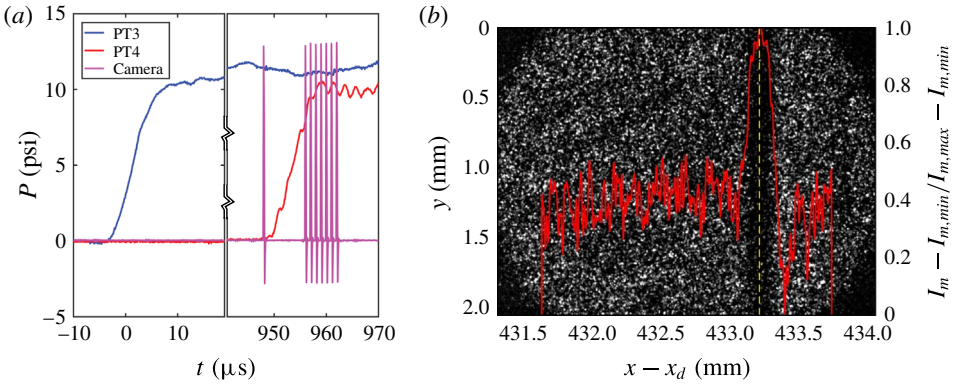


FIGURE 2. (*a*) Time traces of pressure signals from transducers PT3 and PT4 with the framing camera timing and (*b*) sample shadowgraph image superposed with the mean intensity profile (red). The shock location is indicated by a dashed line. Image contrast has been enhanced to better show the shock shadowgraph, and the resulting speckle in the image is background noise, not experimental particles.

3. Results and discussion

The history of particle drag is calculated along the one-dimensional Lagrangian particle trajectories reconstructed from eight independent images. To reconstruct particle trajectories through the entire relaxation zone, we acquire $O(50)$ measurements at different post-shock times. For any given particle, usually four to seven post-shock trajectory images are captured. A large interframe time step (Δt) is optimal for obtaining the particle trajectory through the relaxation time. A small Δt, on the other hand, is optimal for capturing particle displacements during the initial stage of unsteady particle acceleration. We address these opposing criteria by repeating the experiments with multiple time steps ($\Delta t = 0.5$ μs, 1.0 μs and 2.0 μs). The typical image size of a particle is approximately nine pixels across, with average displacement of approximately 50 pixels. The pre-shock particle location is registered in the first frame based on peak intensity, and the particle is tracked using cross-correlation between frames, with an uncertainty of one pixel.

For one-dimensional flows, the relationship between C_D and the physical and kinematic properties of a particle and the post-shock gas reduces to (Igra & Takayama 1993)

$$\frac{\dfrac{\mathrm{d}^2 x_p}{\mathrm{d}t^2}}{\left(u_g - \dfrac{\mathrm{d}x_p}{\mathrm{d}t}\right)^2} = \frac{3\rho_g C_D}{4\rho_p d_p} = \mathcal{A}. \tag{3.1}$$

Here, $\mathrm{d}x_p/\mathrm{d}t$ and $\mathrm{d}^2x_p/\mathrm{d}t^2$ are the velocity and acceleration of the particle; ρ_p and ρ_g are the densities of the particle and post-shock gas. Estimation of C_D directly from (3.1) requires that the time derivatives of position are calculated from each trajectory. However, when calculating the acceleration using numerical differentiation, even a small error in particle locations can lead to substantially large errors (Christensen & Adrian 2002). We avoid differentiation of the experimental data by adopting a method of piecewise fitting of measured particle locations, as described below.

https://doi.org/10.1017/jfm.2017.389 Published online by Cambridge University Press

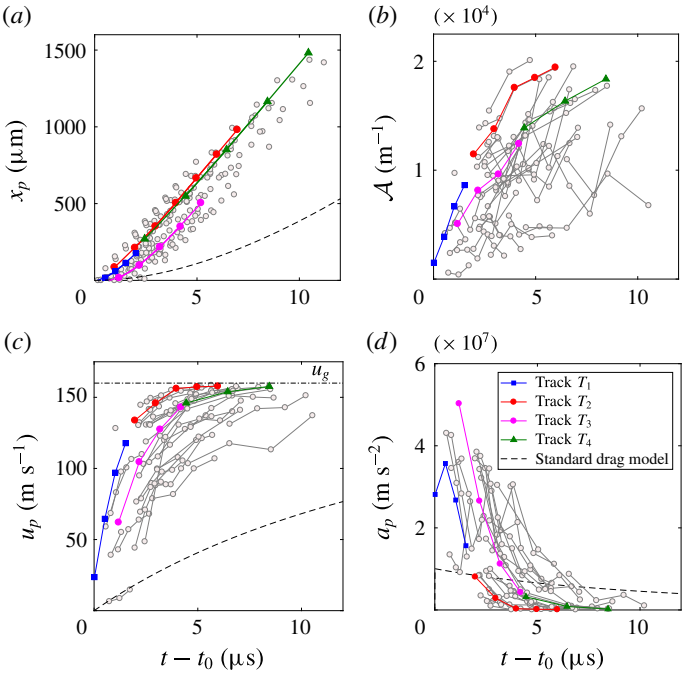


FIGURE 3. (*a*) Particle location (x_p) for $M_s = 1.3$ experiments obtained from particle tracking with $\Delta t = 0.5$ μs, 1.0 μs and 2.0 μs, and the corresponding (*b*) fitting parameter $\mathcal{A}$ (see (3.2)), (*c*) velocity u_p (see (3.3)) with the post-shock gas velocity (u_g, – · – · –) and (*d*) acceleration a_p (see (3.1)) obtained from piecewise nonlinear fitting (—○—). The dashed lines (– – –) show the values expected from Clift–Gauvin drag (3.4). Four individual particle trajectories, T_1–T_4, are highlighted for reference.

Integrating (3.1) twice with initial conditions $u_p = 0$ and $x_p = x_{p,0}$ at $t = t_0$, we obtain

$$x_{p,i} = x_{p,0} + u_g(t_i - t_0) - \frac{\log(\mathcal{A}u_g(t_i - t_0) + 1)}{\mathcal{A}}. \tag{3.2}$$

Since C_D is not known *a priori*, we derive (3.2) by making a first-order approximation that C_D is constant about three successive particle locations ($x_{p,i-1}$, $x_{p,i}$, $x_{p,i+1}$) in a trajectory. Three successive particle locations are piecewise fitted to the fifth order Taylor series expansion of (3.2) with three fitting parameters, $x_{p,0}$, t_0 and $\mathcal{A}$. Before performing the fit, the time axis is shifted to the reference time, $t_0 = t_s - (x_s - x_p)/V_s$, the time when the shock location coincides with the particle position $x_{p,0}$. Here, x_s and x_p are the shock and particle positions at time t_s. The particle drag coefficient C_D at time t_i for each piecewise fit of the trajectory is obtained from the parameter $\mathcal{A}$ (see (3.1)). Through the fitting method, we obtain $n - 2$ instantaneous C_D values for every n available post-shock particle locations.

Figure 3(*a*) shows particle locations (x_p) for 32 trajectories for $M_s = 1.3$. Four example trajectories (T_1–T_4) are highlighted with their corresponding piecewise fits. The fitting parameter $\mathcal{A}$ for each trajectory is shown in figure 3(*b*). The particle velocities (see figure 3*c*) are obtained by invoking parameter $\mathcal{A}$ in the first integral of (3.1),

$$\frac{\mathrm{d}x_p}{\mathrm{d}t} = \frac{u_g^2\mathcal{A}(t - t_0)}{1 + u_g\mathcal{A}(t - t_0)}, \tag{3.3}$$

https://doi.org/10.1017/jfm.2017.389 Published online by Cambridge University Press

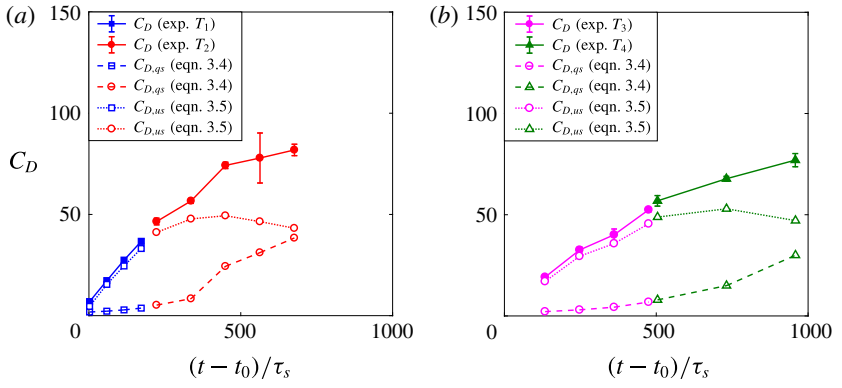


FIGURE 4. The total drag coefficient C_D (solid line), the quasi-steady component $C_{D,qs}$ (dashed line) and the unsteady component $C_{D,us}$ (dotted line) with respect to time normalised by the acoustic time scale (τ_s) for trajectories (*a*) T_1, T_2 and (*b*) T_3, T_4.

and accelerations (see figure 3*d*) are obtained from (3.1). The dashed line in each plot shows the values expected based on standard drag. The particle kinematics captured in figure 3 show the characteristics of the post-shock relaxation zone: (i) the particle acceleration reaches a peak immediately after the shock and then decreases (see figure 3*d*); (ii) the particle velocity continuously increases and asymptotically approaches the post-shock gas velocity (u_g) as the acceleration monotonically approaches zero (see figure 3*c*). The relaxation period is approximately 10 μs or $1000\tau_s$ for these flow conditions.

Drag coefficients for the trajectories T_1, T_2 and T_3, T_4 are shown in figure 4(*a*,*b*). Here, 95 % confidence intervals for C_D are obtained from bootstrapping, with bounds generated via Monte-Carlo simulation. The particle location (x_p), shock speed (V_s) and absolute shock location (x_s) are perturbed over a random Gaussian distribution with standard deviation $\sigma = \Delta p/\sqrt{12}$. The Δp values for x_p, V_s and x_s are 1 pixel, 0.05 m s^{-1} and 0.5 pixel. The C_D at the earliest resolved post-shock time ($\approx 2\tau_s$) is 6.3 (see figure 4*a*). This early-time drag after shock is consistent with the prediction based on the inviscid unsteady model by Parmar *et al.* (2009). This model, validated for stationary particles, predicts that C_D decreases sharply after $t = 2\tau_s$ and attains a constant value equal to the quasi-steady drag after $t \approx 8\tau_s$. Although the acoustic-time drag is consistent with this model, figure 4(*a*,*b*) shows that the particles experience a continuously increasing drag through the relaxation zone. As the particle relaxes into mechanical equilibrium with the background gas, C_D increases by an order of magnitude compared with the time just after shock interaction.

As mentioned in § 1, there are many possible forces that could contribute to the increased drag observed in figure 4. Under shock acceleration, the particle acceleration due to the shock is much larger than gravity, so we assume that $F_g = 0$. The lift force (F_l) is negligible for the smooth spherical particles used in this study, and images show that the particles experience no vertical movement. Elimination of lift and drag effects leaves a combination of quasi-steady (F_{qs}) and unsteady ($F_{us} = F_{iu} + F_{vu}$) forces acting on the particles.

The models that could be used to estimate quasi-steady and unsteady forces (Parmar *et al.* 2009, 2011) are assessed in table 2 for applicability to these experiments. The quasi-steady model is applicable to the HST experiments, but the models for the

https://doi.org/10.1017/jfm.2017.389 Published online by Cambridge University Press

Force model	Model constraint	Present experiment
Quasi-steady (F_{qs})	$Kn \ll 1,\ M_p < 0.6$	$Kn \approx 10^{-2},\ 0.002 \leqslant M_p \leqslant 0.5$
Inviscid unsteady (F_{iu})	$t/\tau_s < 1$	$t/\tau_s \approx 1000$
Viscous unsteady (F_{vu})	$\tau_c Re_p M_s \ll 1$	$210.6 < \tau_c Re_p M_s < 436.8$

TABLE 2. Range of applicability of the models of Parmar *et al.* (2009, 2011) for quasi-steady and unsteady forces compared to experimental values.

unsteady forces are designed for much shorter time scales than the relaxation times we are studying. For the range of particle Mach numbers ($M_p \leqslant 0.5$) and Knudsen numbers ($Kn \approx 0.01$) in this study, the quasi-steady component of the drag coefficient ($C_{D,qs}$) can be estimated using an incompressible model given by the Clift–Gauvin equation (Clift & Gauvin 1970),

$$C_{D,qs} = \frac{24}{Re_p}(1 + 0.15\, Re_p^{0.687}) + 0.42\left(1 + \frac{42\,500}{Re_p^{1.16}}\right)^{-1}. \tag{3.4}$$

To understand how much of the drag in our experiment might be coming from unsteady forces, we estimate the quasi-steady component of drag based on (3.4) and calculate the unsteady component as

$$C_{D,us} = C_{D,experiment} - C_{D,qs}. \tag{3.5}$$

The quasi-steady ($C_{D,qs}$) and unsteady ($C_{D,us}$) components of the drag coefficient for our sample trajectories are shown in figure 4. The quasi-steady force contributes only a small amount to the overall drag at early times, but it increases steadily through the relaxation zone. The combination of decreasing slip between the particle and the surrounding gas, and the large acceleration immediately after the passage of the shock causes some of the high levels of unsteady drag (see (3.1)).

The existing force models for the unsteady components of drag do not predict the large magnitude of $C_{D,us}$ observed in figure 4. The force kernel for the inviscid unsteady component proposed in Parmar *et al.* (2009) decays to zero near $t < \tau_s$, well before the relaxation period (see table 2). The linearised models for the Basset history kernels proposed in Mei *et al.* (1991) and Parmar *et al.* (2011) require a convective time scale $\tau_c \ll 1/(Re_p M_s)$, where $\tau_c = t(u_g - u_p)/d_p$. During the relaxation phase of these experiments, $\tau_c > 1/Re_p$ (see table 2). In this regime, defined by Parmar *et al.* (2011) as 'regime IV: very long time', nonlinear effects become important and the relationship between drag, Re_p and M_s becomes complex (Mei & Adrian 1992; Parmar *et al.* 2011).

To understand the unsteady particle dynamics in the relaxation zone, we examine the drag as a function of a modified Knudsen number, $Kn^* = M_s/Re_p$, for all three Mach numbers, $M_s = 1.2$, 1.3 and 1.4. Figure 5 shows that the variation of C_D with respect to Kn^* is weakly sensitive to M_s within the range of our experiments. With $C_D \propto a_p/Re_p^2$ and the behaviour of a_p shown in figure 3(*d*), we choose a second-order power-law expression $C_D = a - bKn^{*c}$ for a least-squares fit to the data, with $a = 167.5$, $b = 92.2$ and $c = -0.18$ for the range of $Kn^* = 0.04$–3.92. The bounds of this fit, shown in light grey solid and dashed lines, are predicted using simultaneous functional and observational bounds with 95 % confidence validated with Monte-Carlo simulations.

https://doi.org/10.1017/jfm.2017.389 Published online by Cambridge University Press

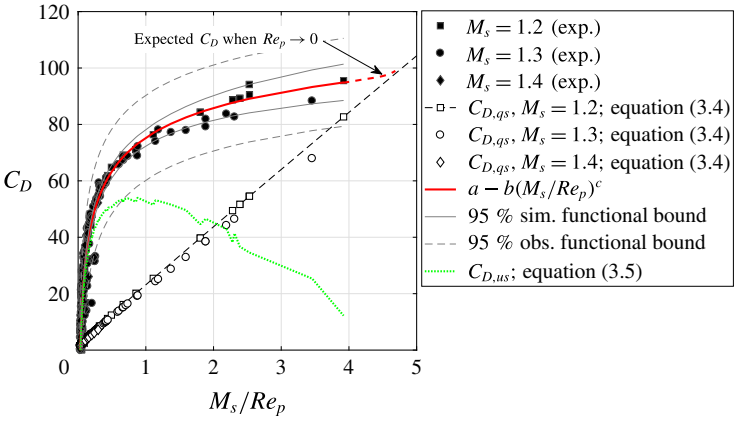


FIGURE 5. Total drag coefficient C_D, quasi-steady ($C_{D,qs}$) and unsteady ($C_{D,us}$) components with respect to M_s/Re_p. The red line is a least-squares fit to the experimental data, $C_D = a - b(M_s/Re_p)^c$, with $a = 167.5$, $b = 92.2$ and $c = -0.18$. The grey solid and dashed lines are simultaneous functional and observational 95 % confidence bounds.

For the experimentally measured data with all three incident Mach numbers, we can again calculate the contributions from the quasi-steady model ((3.4), as shown in figure 5), with the remaining unsteady drag contribution shown by the green dotted line in figure 5. Here, $C_{D,us}$ is the primary contributor to the overall drag until $Kn^* \approx 1$, with maximum values in the range $0.5 \leqslant Kn^* \leqslant 1.0$. For all Mach numbers, $C_{D,qs}$ increases almost linearly through the relaxation period. After $Kn^* \approx 1.0$, the unsteady force contribution declines, and it intersects the increasing quasi-steady force contribution at $Kn^* \approx 2$.

As indicated in table 1, our data are limited to $Re_p > 0.3$. As $Re_p \to 0$, the total drag should approach the Stokes flow regime, when the quasi-steady drag will completely dominate the total drag. This trend is shown with a dashed red line in figure 5, where the red empirical curve is connected to the Mach 1.3 quasi-steady (black dashed) line.

4. Conclusions

The unsteady drag coefficients of shock accelerated microparticles through the relaxation period are higher than the drag coefficients predicted by either standard drag or any current quasi-steady and unsteady drag models. The high drag coefficients measured just after shock passage (near the acoustic time scales) agree with the drag coefficients reported in previous studies, but the measured drag coefficients at later times quickly exceed model predictions. The coefficient of drag is highly sensitive to the time-dependent particle slip velocity. This dependence, represented by a modified time-dependent Knudsen number, $Kn^* = M_s/Re_p$, results in a power-law behaviour of the unsteady drag coefficient. The increased drag is caused by unsteady forces that are not approximated by current linearised models, and these forces are higher than the quasi-steady drag until $Kn^* \approx 2$. Because the physical mechanisms affecting drag are coupled in a nonlinear way during the relaxation time period, it is difficult to assess how the time-dependent drag will change when there are compressibility effects ($M_p > 0.6$), or whether there are other additional forces such as temperature changes or particle deformation at higher Mach numbers. Simulations may provide some insights into these complex dynamics.

https://doi.org/10.1017/jfm.2017.389 Published online by Cambridge University Press

References

ANDERSON, J. D. 1990 *Modern Compressible Flow*, 2nd edn. McGraw-Hill.

BOIKO, V. M., KISELEV, V. P., KISELEV, S. P., PAPYRIN, A. N., POPLAVSKY, S. V. & FOMIN, V. M. 1997 Shock wave interaction with a cloud of particles. *Shock Waves* **7**, 275–285.

CHRISTENSEN, K. T. & ADRIAN, R. J. 2002 Measurement of instantaneous Eulerian acceleration fields by particle image accelerometry. *Exp. Fluids* **33**, 759–769.

CLIFT, R. & GAUVIN, W. H. 1970 The motion of particles in turbulent gas streams. *Proc. Chemeca'70* **1**, 14–28.

GENG, J. H. & GROENIG, H. 2000 Dust suspensions accelerated by shock waves. *Exp. Fluids* **28**, 360–367.

GORE, R. & CROWE, C. 1989 Effect of particle size on modulating turbulent intensity. *Intl J. Multiphase Flow* **15** (2), 279–285.

HENDERSON, C. 1976 Drag coefficients of spheres in continuum and rarefied flows. *AIAA J.* **14** (6), 707–708.

IGRA, O. & TAKAYAMA, K. 1993 Shock tube study of the drag coefficient of a sphere in a non-stationary flow. *Proc. R. Soc. Lond.* A **442**, 231–247.

JOURDAN, G., HOUAS, L., IGRA, O., ESTIVALEZES, J. L., DEVALS, C. & MESHKOV, E. E. 2007 Drag coefficient of a sphere in a non-stationary flow: new results. *Proc. R. Soc. Lond.* A **463**, 3323–3345.

KULICK, J. D., FESSLER, J. R. & EATON, J. K. 1994 Particle response to turbulence modification in fully developed channel flow. *J. Fluid Mech.* **277**, 109.

LONGHORN, A. L. 1952 The unsteady, subsonic motion of a sphere in a compressible inviscid fluid. *Q. J. Mech. Appl. Maths* **5**, 64–81.

LOTH, E. 2008 Compressibility and rarefaction effects on drag of a spherical particle. *AIAA J.* **46** (9), 2219–2228.

MAGNAUDET, J. & EAMES, I. 2000 The motion of high-Reynolds-number bubbles in inhomogeneous flows. *Annu. Rev. Fluid Mech.* **32**, 659–708.

MARTINEZ, A. A., ORLICZ, G. C. & PRESTRIDGE, K. P. 2015 A new experiment to measure shocked particle drag using multi-pulse particle image velocimetry and particle tracking. *Exp. Fluids* **56**, 1854.

MAXEY, M. R. & RILEY, J. J. 1983 Equation of motion for a small rigid sphere in a nonuniform flow. *Phys. Fluids* **26** (4), 883.

MEI, R. & ADRIAN, R. J. 1992 Flow past a sphere with an oscillation in the free-stream velocity and unsteady drag at finite Reynolds number. *J. Fluid Mech.* **237**, 323–341.

MEI, R., LAWRENCCE, J. & ADRIAN, R. J. 1991 Unsteady drag on a sphere at finite Reynolds number with small fluctuations in the free-stream velocity. *J. Fluid Mech.* **233**, 613–631.

MEJIA-ALVAREZ, R., WILSON, B., LEFTWICH, M. C., MARTINEZ, A. A. & PRESTRIDGE, K. P. 2015 Design of a fast diaphragmless shock tube driver. *Shock Waves* **25** (6), 635–650.

MILES, J. W. 1951 On virtual mass and transient motion in subsonic compressible flow. *Q. J. Mech. Appl. Maths* **4**, 388–400.

MIURA, H. & GLASS, I. I. 1983 On the passage of a shock wave through a dusty-gas layer. *Proc. R. Soc. Lond.* A **385**, 85–105.

MURAKAMA, T. & ISHIKAWA, M. 1978 Holographic measurements of velocity distribution of particles accelerated by a shock wave. In *Proceedings of the 13th International Congress on High Speed Photography and Photonics, Proc. SPIE 0189*, pp. 326–329.

PARMAR, M., HASELBACHER, A. & BALACHANDAR, S. 2008 On the unsteady inviscid force on cylinders and spheres in subcritical compressible flow. *Phil. Trans. R. Soc. Lond.* A **366**, 2161–2175.

PARMAR, M., HASELBACHER, A. & BALACHANDAR, S. 2009 Modeling of the unsteady force for shock–particle interaction. *Shock Waves* **19**, 317–329.

PARMAR, M., HASELBACHER, A. & BALACHANDAR, S. 2010 Improved drag correlation for spheres and application to shock-tube experiments. *AIAA J.* **48**, 1273–1276.

https://doi.org/10.1017/jfm.2017.389 Published online by Cambridge University Press

PARMAR, M., HASELBACHER, A. & BALACHANDAR, S. 2011 Generalized Basset–Boussinesq–Oseen equation for unsteady forces on a sphere in a compressible flow. *Phys. Rev. Lett.* **106**, 084501.

RUDINGER, G. 1964 Some properties of shock relaxation in gas flows carrying small particles. *Phys. Fluids* **7** (5), 658–663.

RUDINGER, G. 1970 Effective drag coefficient for gas–particle flow in shock tubes. *Trans. ASME J. Basic Engng* **92**, 165–172.

SAITO, T., SABA, M., SUN, M. & TAKAYAMA, K. 2007 The effect of an unsteady drag force on the structure of a non-equilibrium region behind a shock wave in a gas–particle mixture. *Shock Waves* **17**, 255–262.

SETTLES, G. S. 2006 *Schlieren and Shadowgraph Techniques*. Springer.

SMOLDERS, H. J. & VAN DONGEN, M. E. H. 1992 Shock wave structure in a mixture of gas, vapour and droplets. *Shock Waves*.

SOMMERFELD, M. 1985 The unsteadiness of shock waves propagating through gas–particle mixtures. *Exp. Fluids* **3**, 197–206.

STRECKER, J. J. F. & ROTH, P. 1994 Particle breakup in shock waves studied by single particle light scattering. *Part. Part. Syst. Charact.* **11**, 222–226.

SUN, M., SAITO, T., TAKAYAMA, K. & TANNO, H. 2005 Unsteady drag on a sphere by shock wave loading. *Shock Waves* **14** (1), 3–9.

TANAKA, T. & EATON, J. K. 2010 Sub-Kolmogorov resolution particle image velocimetry measurements of particle-laden forced turbulence. *J. Fluid Mech.* **643**, 177–206.

WAGNER, J., BERESH, S., KEARNEY, S., PRUETT, B. & WRIGHT, E. 2012 Shock tube investigation of quasi-steady drag in shock–particle interactions. *Phys. Fluids* **24**, 123301.

https://doi.org/10.1017/jfm.2017.389 Published online by Cambridge University Press